Available online at www.sciencedirect.com
SCIENCE DIRECT®
International Journal of Thermal Sciences 42 (2003) 847–855
International Journal of Thermal Sciences
www.elsevier.com/locate/ijts

Microfluidic velocimetry with near-wall resolution

David A. Sinton, Dongqing Li *

Department of Mechanical and Industrial Engineering, University of Toronto, 5 King's College Road, Toronto, ON, Canada M5S 3G8

Received 24 July 2002; accepted 5 November 2002

Abstract

A combined experimental and numerical analysis technique for velocity profiles with near-wall resolution in liquid microchannel flows is described. The working fluids employed are aqueous solutions with caged fluorescent dyes. A sheet of fluorescent dye is photo-injected by briefly exposing a cross-section of the fluid to ultraviolet light. The transport of the resulting 'band' of fluorescent dye is imaged onto a CCD camera using an epi-illumination fluorescent microscope system. The velocity profile is calculated from images acquired and processed after each uncaging event. Results are shown to compare favorably to analytical solutions in both pressure-driven and electroosmotic flow in circular cross-section capillaries. Near-wall resolution is verified through application to electroosmotic flows with thin electrical double layers. The ability of the technique to collect velocimetry data up to 2.5 μm from the wall is demonstrated.

Keywords: Microchannel; Flow; Visualization; Electroosmotic; Near-wall resolution

1. Introduction

Recent advances in manufacturing have made possible the fabrication of micro-sized fluidic devices. Micro-sized chemical synthesis and analysis systems can offer many advantages over their traditional, macro-sized counterparts due to the increase in surface area to volume ratio accompanying miniaturization. Most often, advantages stem from a reduction in sample volume and processing time. These improved capabilities are mainly products of the enhanced heat dissipation characteristics of microfluidic chips over their macro-sized counterparts. The fluid flow and heat transfer phenomena are coupled in these lab-on-a-chip applications, in that both the rate of fluid flow and the rate of heat generation (by Joule heating) are functions of the applied electrical field. Direct micro-flow visualization for determination of the fluid velocity profile plays a key role in the study of these phenomena. Although much effort has been devoted to microfluidic chip-based design, relatively little is known about the underlying physics of microflows.

Various methods for microflow visualization have evolved, often through the adaptation of well-developed macroflow visualization methods such as particle image velocimetry (PIV). Application of PIV to microflows typically involves use of fluorescent microspheres due to the submicrometer particle sizes required. Taylor and Yeung [1] calculated fluid velocity from the streaks produced from fluorescent particles in a liquid flow in a capillary. More recently, PIV techniques involving double-frame cross-correlation algorithms have been successfully applied to microflows [2,3]. The hydrophobicity of latex particles, a common choice of marker in PIV, can cause particle aggregation and adhesion to the channel surface. The use of hydrophilic markers, such as the unilamellar liposomes employed recently by Singh et al. [4], can mitigate these effects. Extracting an unaltered local fluid velocity from an observed marker velocity, however, remains a fundamental challenge in PIV and flow visualization techniques in general. This is further complicated on the microscale by the addition of electrokinetic effects including electrophoresis, electrophoretic relaxation, and particle-wall interactions [5]. Recently, a second-order accurate cross-correlation algorithm was shown to improve near-wall resolution of PIV techniques [6].

Dye-based microflow visualization techniques have also evolved from their macro-sized counterparts. Dye can be directly injected into many macroscale flow situations without significantly altering the flow pattern. However, these mechanical injection techniques are difficult to apply on the microscale without interfering with the flow field. One option is to replace a solution with a dye solution and track the

* Corresponding author.
E-mail address: dli@mie.utoronto.ca (D. Li).

1290-0729/$ – see front matter
doi:10.1016/S1290-0729(03)00057-7

Nomenclature

c_i	concentration of species i	M	
D	diffusion coefficient	$m^2 \cdot s^{-1}$	
E	electric field strength	$V \cdot m^{-1}$	
e	charge of a proton	C	
j_i^*	molar flux of species i	$M \cdot m \cdot s^{-1}$	
k	Boltzmann constant	$J \cdot K^{-1}$	
mag	magnification		
N	number of images		
n	number of velocity profiles		
n_{ref}	index of refraction		
NA	numerical aperture		
R	inner radius of capillary	m	
r	radial coordinate	m	
T	absolute temperature	K	
Δt	timestep between exposures	s	
u_E	electroosmotic velocity	$m \cdot s^{-1}$	
u_{ob}	observed velocity of the dye	$m \cdot s^{-1}$	
u_P	centerline velocity in Poiseuille flow	$m \cdot s^{-1}$	
u_{ph}	electrophoretic velocity of the dye	$m \cdot s^{-1}$	
u_x	mass averaged velocity in axial direction	$m \cdot s^{-1}$	
x	axial coordinate	m	
z_i	ionic valence of species i		

Greek symbols

δ	Debye length	m
λ	wavelength	m
ν_E	electroosmotic mobility	$m^2 \cdot V^{-1} \cdot s^{-1}$
ν_{ph}	electrophoretic mobility	$m^2 \cdot V^{-1} \cdot s^{-1}$
ξ	zeta potential	V
Ψ	local electrostatic potential	V

concentration front [1,5]. These methods are complicated by the relatively fast diffusion at the dye front, and the changes in the EDL due to differences between the dye solution and the original solution. In addition, accurate tracking usually requires high concentration gradients, which in turn, generate high rates of diffusion relative to the mean flow velocity. Tracking points of zero concentration gradient (maxima) would minimize diffusion effects, however, these points are not clearly definable when one solution is gradually replaced with another.

Specialized caged fluorescent dyes can serve to eliminate the problems associated with mechanical dye injection. A photo-injection is accomplished by exposing an initially non-fluorescent solution seeded with caged fluorescent dye to ultraviolet light. As a result of ultraviolet exposure, caging groups are broken and fluorescent dye molecules are released [7]. The free fluorescent dye may then be imaged using classical fluorescence techniques. Lempert et al. [8] applied caged dyes to flow visualization in a 1 cm i.d. pipe as well as a large water channel facility. Paul et al. [9] applied the method to microflow visualization. In that study, images of dye transport in pressure-driven flow and electrokinetically-driven flow were presented. Velocity profiles were calculated for the pressure-driven case using image pairs and a scalar image velocimetry (SIV) technique. That study outlined several key issues associated with caged-dye techniques on the microscale, namely: decreasing signal to noise ratio near the wall; and predicting electrophoretic motion of the charged dye molecules (especially problematic in large molecular weight, multi-component dyes). Dye-based velocimetry requires knowledge of the electrophoretic mobility of the dye molecules when the method is applied to electrokinetic flows (analogous to PIV). Recently, Herr et al. [10] applied the method of Paul et al. [9] to study capillary flow with nonuniform zeta potential. Herr et al. [10] tracked the motion of the dye by fitting Gaussian curves to the axial concentration profiles. More generally, Dahm et al. [11] presented a SIV technique for four-dimensional, turbulent velocity field measurements. With the benefit of these findings [8–11] and our own tests, we have developed a microchannel flow visualization system and complimentary analysis technique. We present both pressure-driven as well as electrokinetically-driven velocity profiles comparing well with analytical results and those of previous experimental studies. A key aspect of the method described here is the degree of near-wall resolution achieved that has not previously been reported in dye-based microflow visualization studies.

In our experiment, ultraviolet laser light is focused into a sheet crossing the capillary (perpendicular to the flow direction). The resulting fluorescent dye is continuously excited and the emission is transmitted through a laser-powered epi-illumination microscope. Full frame images of the transport are recorded by a progressive scan CCD camera and saved automatically on the computer. In the numerical analysis, the images are processed and cross-stream velocity profiles are calculated based on tracking the dye concentration maxima through a sequence of several consecutive images. Several sequential images are used to improve the signal to noise ratio. Points of concentration maxima make convenient velocimetry markers as they are resistant to diffusion. In many ways, the presence of clearly definable, zero-concentration-gradient markers is a luxury afforded by the photo-injection process.

2. Experiment

2.1. Imaging apparatus

A labeled photograph of the system is provided in Fig. 1. The two required laser beams were fixed and ran

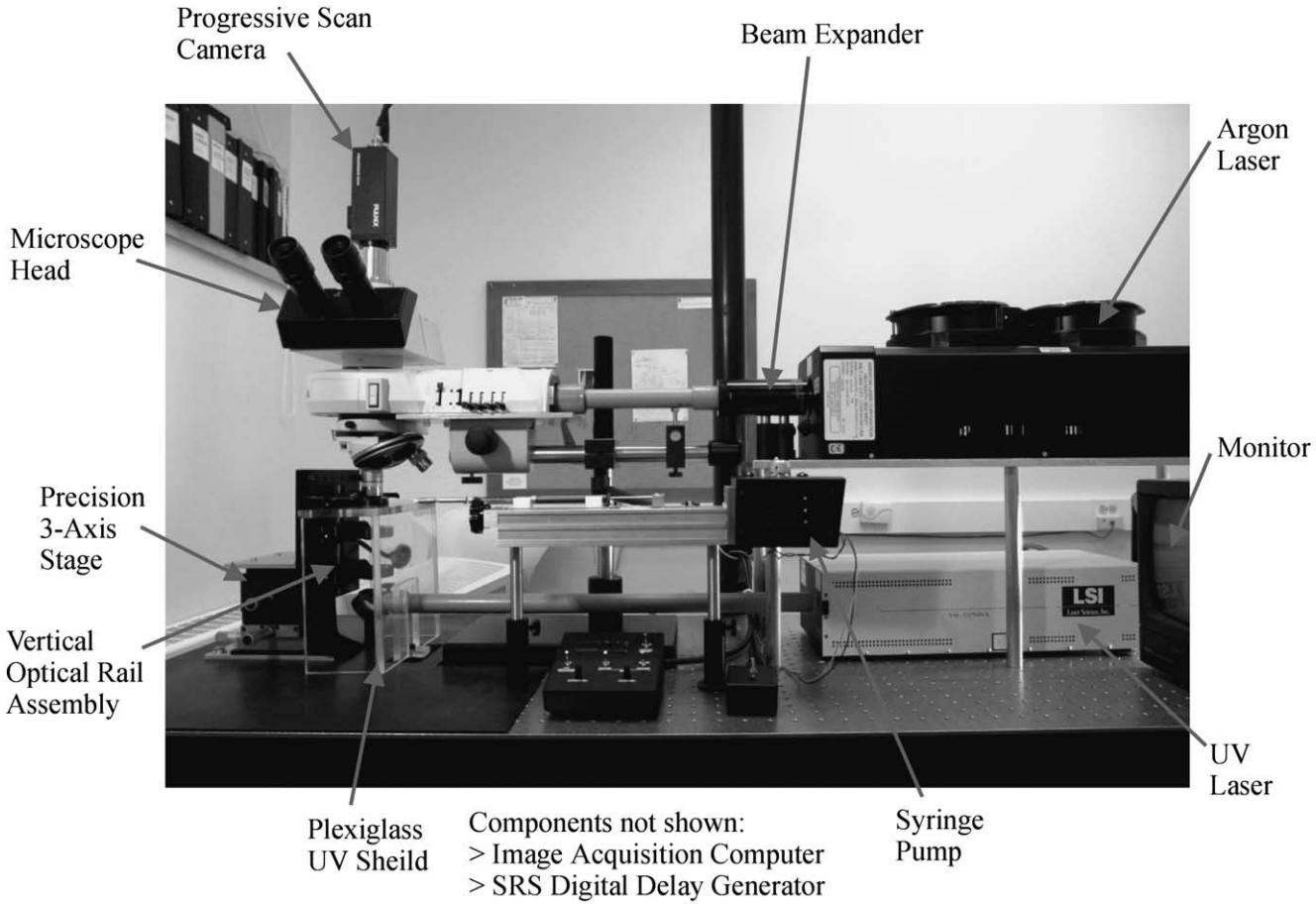

Fig. 1. Imaging apparatus.

horizontal and parallel: the blue, excitation beam above; and the ultraviolet beam below. The ultraviolet light was provided by a 300 μJ, $\lambda = 337$ nm, pulsed nitrogen laser (LSI, VSL-337ND-S). This beam was reflected upwards by a stationary mirror and through a vertical optical rail assembly containing two consecutive, counter-oriented, cylindrical optics followed by a blank optic on which the capillary rested (all of which were fused silica). The first cylindrical optic ($f = 100$ mm plano convex) focused the beam into a sheet. The second cylindrical optic ($f = 50$ mm plano convex) condensed this sheet into the capillary in the cross-stream direction. All three optics were adjusted relative to each other on the vertical optical rail. The rail itself, including the flow module was mounted on a precision three-axis stage.

A single-line, 200 mW, $\lambda = 488$ nm argon laser (American Laser Corp., LS300B) provided a continuous flood of excitation light through the objective. The laser beam passed through a 10× beam expander before entering the epi-fluorescent microscope head (Leica DMLM). The original, lamp-based optics in the microscope were removed to facilitate collimated light, and no excitation filter was required as the light was monochromatic. The beam is reflected off a dichroic mirror ($\lambda = 510$ nm long pass) directly into the oil immersion, 25× objective with numerical aperture, $NA = 0.75$ (Leica PL Fluotar). High numerical aperture objectives are especially desirable in weak signal, epi-illumination applications. Inoue and Spring [12], report received signal intensities varying with numerical aperture and magnification as follows:

$$I = NA^4/mag^2 \tag{1}$$

Other advantages of high *NA* include reduced depth of field and increased resolution, often at the expense of working distance [12]. The Abbe spatial resolution of this apparatus was approximately 1.2 μm in the object plane, and the depth of field was calculated as 2.1 μm. A single drop of optical oil surrounded the windowed portion of the capillary and connected directly to both the objective and the blank base optic. This full immersion design provided index matching for imaging and both the excitation and ultraviolet light. Cargille (FF) optical oil was used due to its ultra-low fluorescence and an index of refraction, $n_{\text{ref}} = 1.485$, similar to that of the fused silica, $n_{\text{ref}} = 1.46$. The received fluorescent signal passed through the dichroic mirror and through an additional suppression filter ($\lambda = 515$ nm long pass) to the 2/3 progressive scanning interline transfer CCD camera (Pulnix, TM-9701). Progressive scan architecture enabled all pixels in the CCD array to be exposed concurrently with all data

being subsequently transferred (in contrast to even and odd field interlacing). This is desirable from an image quality perspective, however, when running in this mode the signal could only be viewed through the computer. The video monitor required signals in interlaced mode and could only be used for focusing and alignment. Images received by the camera were digitized and saved automatically through a PC-based image acquisition system. Full frame images could be collected at rates up to 30 Hz.

2.2. Image acquisition

A four-channel delay generator (SRS, DG535) controlled the firing of the nitrogen laser, run frequency, and synchronization with the camera when necessary. The system could be run in two modes:

(1) The camera was asynchronously reset by the delay generator a set time after the laser had been fired; and
(2) The camera was run in video mode and the delay generator fired the laser at convenient intervals. To increase the amount of uncaged dye, the nitrogen laser could be pulsed multiple times (to a maximum rate of 60 Hz) at each uncaging event.

The number of pulses per uncaging event is restricted only by fluid velocity and the desired sheet thickness. The excitation laser ran unshuttered, continuously flood-illuminating the capillary. Image exposure durations were controlled using electronic shuttering modes in the camera. The acquired images had a resolution of 640×484 pixels. This corresponded to a viewing area of 346×261 μm with each pixel representing a 0.54 μm square. A $1\times$ c-mount was employed such that this magnification is only a consequence of the objective magnification and the size of the CCD array.

2.3. Image processing

To remove any non-uniformities present in the imaging system, dark field image subtraction and bright field image normalization were performed [12]. A dark field image (or background image) for each run was taken immediately before the laser was fired. This dark field image contained a faint signal from stray background light as well as fluorescent emission from trace amounts of uncaged dye in the bulk fluid. Before a bright field image was taken, the flow was stopped and the nitrogen laser was fired repeatedly until uncaged dye had diffused well beyond the camera's field of view. Using a Matlab program, the dark field image was subtracted from all images including the bright field image. These images were then normalized with respect to this bright field image and smoothed using a distance-based 7×7 pixel kernel. This kernel size corresponds to a 3.2 μm square in the object plane, such that pixel intensity values could influence neighbors up to 1.62 μm away in each radial and axial direction. Finally, the resulting image series was linearly scaled by a single factor so as to fill the grayscale range.

2.4. Flow systems

A custom designed, ultra-low flow rate syringe pump provided pressure-driven flow. A DC micromotor was required to ensure a continuous flow rate, not achievable with commercial designs based on stepper motors. For electroosmotic flow, a separate, two-reservoir flow module was used. A 14 cm long capillary liquid junction joined the small reservoirs with embedded platinum electrodes. The capillary and both reservoirs were filled with the same caged dye solution before any voltage was applied. All capillaries were fused silica with exterior polymide coating as supplied by Polymicro Tech. The nominal inner diameters of the capillaries were 100 μm and 205 μm. However, using an electron microscope the inner diameters were found to be 102 μm and 205 μm. Each capillary was prepared by flushing with pure water, followed by filtered buffer. The exterior polyimide coating was oxidized and removed to create a viewing window.

Since only minute amounts were involved in uncaging events, most dye was used in filling the flow system. The cost of specialized caged dyes was such that careful design of these systems reduced operating costs significantly. Several minutes of pressure-driven flow and electrokinetically-driven flow was facilitated with less than 10 μL and 50 μL, respectively.

2.5. Chemicals

Two caged fluorescent dyes, supplied by Molecular Probes, were employed here: 5-carboxymethoxy-2-nitrobenzyl (CMNB)-caged fluorescein (826.81 MW); and 4,5-dimethoxy-2-nitrobenzyl (DMNB)-caged fluorescein dextran (10000 MW). Both dyes were dissolved in sodium carbonate buffer of $\mathrm{pH} = 9.0$. The buffer was prepared by dissolving 39.8×10^{-3} mol of $NaHCO_3$ and 3.41×10^{-3} mol of Na_2CO_3 in 1 litre of pure water resulting in a solution of ionic strength, $I = 0.05$. Stock solutions of DMNB-caged fluorescein dextran and CMNB-caged fluorescein were prepared in 0.2 mM and 1 mM concentrations, respectively. The solutions were aliquoted and stored in darkness at $-20\,^{\circ}\mathrm{C}$. Immediately before use, all solutions were filtered using 0.2 μm pore size syringe filters.

Both caged dyes release fluorescein upon photolysis which has an absorption maximum at approximately $\lambda = 490$ nm and is well suited to excitation with the $\lambda = 488$ nm output line of the argon laser. DMNB caging groups absorb light most efficiently from $\lambda = 340$ nm to $\lambda = 360$ nm. CMNB caging groups, however, exhibit an absorption maximum at $\lambda = 334$ nm which is very well suited to the $\lambda = 337$ nm output of a nitrogen laser.

3. Results and discussion

To facilitate the multiple-image analysis technique, all results presented here were acquired using mode 2 in which the camera ran in progressive scan video mode and the delay generator controlled the ultraviolet laser. The nitrogen laser was triple-pulsed at 30 Hz at each uncaging event. The overall run frequency was set to 0.15 Hz, providing more than sufficient time for uncaged dye to exit the field of view. The camera was run at 15 Hz resulting in 100 stored images per uncaging event. Individual exposure times were 1/125 sec (corresponding to shutter mode 8 on the TM-9701). The timescale over which the uncaging process occurs is also an important consideration. In general, this delay can vary from microseconds to seconds [7]. Here, dye release was effectively complete 50 msec after the uncaging event, and only images taken after this period were used in velocimetry calculations. This delay corresponds to the first major timescale of dye release found by Lempert et al. [8].

3.1. Numerical analysis technique

Although the mass-weighted average velocity, $\vec{u}$, is of interest, only the transport of the uncaged dye ions is observed. The numerical analysis technique must infer the mass-weighted average velocity, $\vec{u}$, from images of ion transport which can differ from the advective transport due to forced and ordinary diffusion. The molar flux of uncaged dye ions, $\vec{j}_i^*$, is governed by the Nernst Planck equation in the form

$$\vec{j}_i^* = c_i \vec{u} - D \vec{\nabla} c_i - \left(\frac{z_i e}{kT}\right) D c_i \vec{\nabla} \Psi \tag{2}$$

where Ψ is the electrostatic potential. If the flow is fully developed, and the axial gradient of the electrostatic potential is a known constant, E_x, the axial electrophoretic velocity, u_{ph}, becomes a known constant and the ionic flux takes the form

$$\left(j_i^*\right)_x = c_i(u_x + u_{\mathrm{ph}}) - D\frac{\partial c_i}{\partial x} \tag{3}$$

(With respect to the special case of pressure-driven flow in the presence of a thin EDL, the streaming potential becomes insignificant and the electrophoretic velocity, u_{ph}, may be neglected.)

In locations where the concentration gradient is zero, the observed ionic transport is only the addition of a known electrophoretic velocity and the desired, mass-weighted averaged velocity. In this method, each of these locations of zero axial dye concentration gradient were chosen as marker points, such that the cross-sectional velocity profile could be calculated directly from the observed velocity of these points as follows:

$$u_x(r) = u_{\mathrm{ob}}(r) - u_{\mathrm{ph}} \tag{4}$$

Before each run, the camera was rotated such that the pixel grid was aligned with the radial and axial directions. After each run, the received images were processed and read into the analysis program in matrix format. Along each axial line of pixels, a zero gradient marker point was located using a weighted average of the highest intensity values on that line. The set of markers from each image formed a cross-stream, maximum concentration profile. Any pair of these profiles could provide a velocity profile by dividing the distance between them, Δx, by the corresponding timestep, Δt. With 8 images, 28 velocity profiles could be constructed. In general, for a set of N images a set of n velocity profiles could be constructed where

$$n = \sum_{i=1}^{N}(N - i) \tag{5}$$

Here, all n displacements were calculated and an error-weighted average technique was applied to calculate the velocity profile. The basis of the weighting was that displacement measurements, Δx_i, would all have similar error due to finite, random, signal noise. The size of the corresponding timestep, however, would scale the effect of that error on the velocity value. Weighting each measurement such that each contributed equally to the overall error resulted in the straightforward calculation below

$$u_x(r) = \frac{\sum_{i=1}^{n} \Delta x_i(r)}{\sum_{i=1}^{n} \Delta t_i} \tag{6}$$

3.2. Pressure-driven flow

In the absence of an applied electric field and any electro-viscous effects, pressure-driven flow in a circular cross-section capillary results in a parabolic profile of the form

$$u_x = u_{\mathrm{P}}\left(1 - \left(\frac{r}{R}\right)^2\right) \tag{7}$$

where u_{P} is the velocity at the centerline. Images of a pressure-driven flow in a 205 μm i.d. capillary are shown in Fig. 2. The DMNB-caged fluorescein dextran in the sodium carbonate buffer was used. Although it is difficult to calculate the exact concentration of dissociated sodium ions, the ionic strength of $I = 0.05$ would indicate a bulk counter-ion concentration on the order of 10^{-2} M at minimum. This is a relatively high ion concentration with respect to electrokinetic effects. An estimate of the Debye length from classical theory [5] gives $\delta = 3$ nm. A conservative estimate of EDL thickness is four Debye lengths. This corresponds to a thickness on the order of 10 nm, which is significantly smaller than the maximum achievable resolution of a light microscope. Such an EDL thickness is sufficiently thin to ensure negligible electro-viscous effects, so that the velocity profile can be expected to remain parabolic right up to the wall.

Fig. 3(a) shows plots of the relative signal intensity (along the centerline of the capillary) vs. axial distance for 8 consecutive images. The points of zero axial concentration gradient correspond to peaks in signal intensity. Profiles of

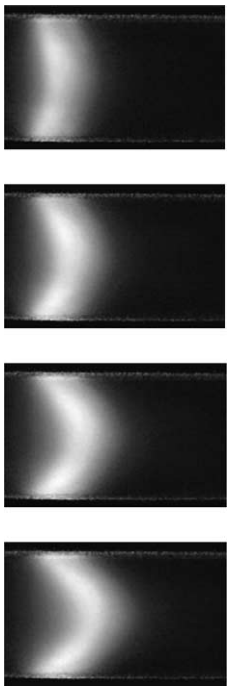

Fig. 2. Images of the uncaged dye in pressure-driven flow through 205 μm i.d. capillary at 133 msec intervals.

concentration maxima calculated along each row of pixels in each image are shown in Fig. 3(b). Applying the numerical analysis technique to these profiles resulted in the velocity data (points) plotted with the parabolic analytical solution (line) in Fig. 3(c). The parabola was calculated assuming a zero-slip velocity at the wall, and a centerline velocity equal to that determined experimentally. The velocity profile is in good agreement with the parabolic analytical solution up to 8 microns from each wall ($r/R = 0.92$). Paul et al. [9] also showed a strong parabolic trend but only data for $-0.5 < r/R < 1$ is displayed due to an insufficient signal-to-noise ratio near the one wall. Near the other wall the reported profiles show a large scatter beyond $r/R = 0.80$. The symmetry of the full cross-section velocity profile given here in Fig. 3(c) is also noteworthy and demonstrates the effectiveness of this method. In future, both halves could be averaged to further increase accuracy.

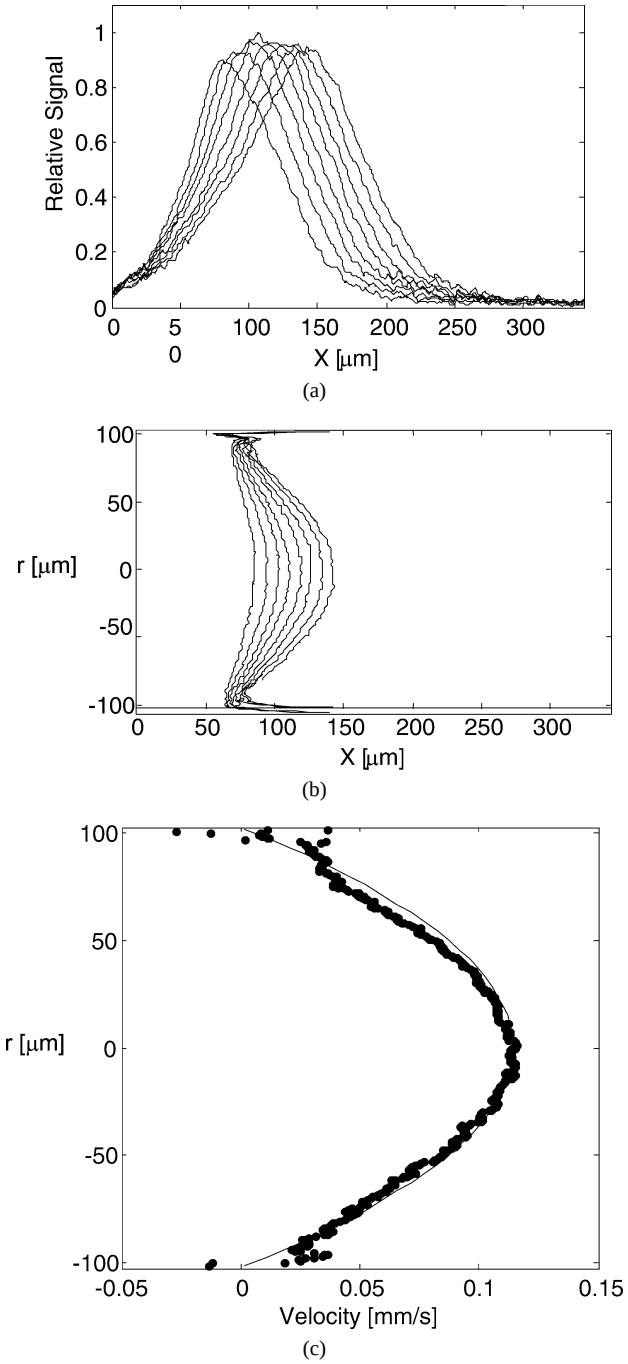

Fig. 3. Data from 8 consecutive images (taken at 15 Hz) of uncaged dye in a pressure-driven flow through a 205 μm i.d. capillary: (a) Plots of relative signal intensity (along the centerline) vs. axial distance for all images; (b) Plots of concentration maxima for all images; and (c) Calculated velocity (points) plotted with parabolic analytical solution.

3.3. Electroosmotic flow

The two reservoirs in the flow module were carefully balanced in order to avoid pressure-driven flow. In addition, both reservoirs contained the dye solution so that the system could be left for several minutes and allowed to come into equilibrium. In early tests, it was found that the fluorescein dextran dye performed poorly in electroosmotic flows. Paul et al. [9] suggested that the multi-component nature of this dye make it unsuitable for these applications. Here, the CMNB-caged fluorescein with the sodium carbonate buffer and 102 μm i.d. capillaries were used in all electroosmotic flows. Images of the uncaged dye transport in four different electroosmotic flows are displayed in vertical sequence in Fig. 4. To ensure the flow was quiescent, a run was completed before the electrical field was applied. The dye diffused symmetrically as shown in Fig. 4(a). Image sequences given in Figs. 4(b), (c), and (d) were taken with voltages of 1000 V, 1500 V, and 2000 V, respectively (over the 14 cm length of capillary). The field was applied with

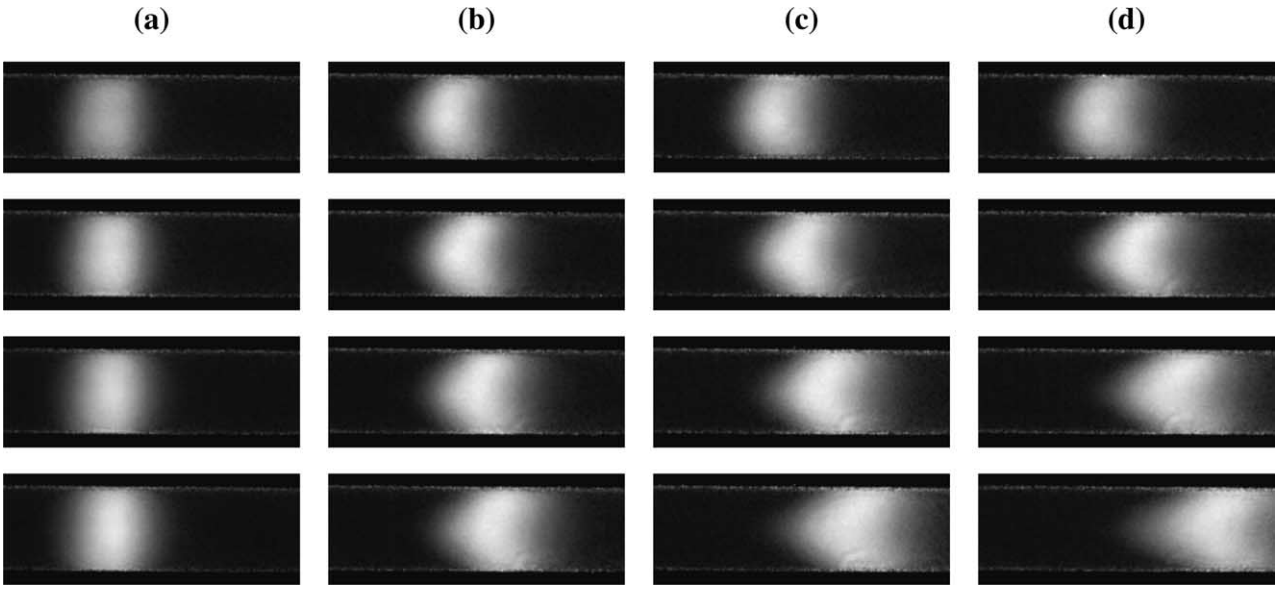

Fig. 4. Images of the uncaged dye in electroosmotic flows through a 102 μm i.d. capillary at 133 msec intervals with applied electric fields of strengths: (a) 0 V/0.14 m; (b) 1000 V/0.14 m; (c) 1500/0.14 m; and (d) 2000 V/0.14 m.

positive at left and negative at right. The resulting plug-like motion of the dye is characteristic of electroosmotic flow in the presence of a negatively charged surface at high ionic concentration. The cup-shape of the dye profile was observed to happen in cases (b), (c), and (d) within the first 50 msec following the ultraviolet light exposure. This period corresponded to the uncaging timescale in which the most significant rise in uncaged dye concentration occurs. Although the exact reason for the formation of this shape is unknown, it is likely that it was an artifact of the uncaging process in the presence of the electric field. Fortunately, however, the method is relatively insensitive to the shape of the dye concentration profile. Once formed, it is the transport of the concentration profile that provides the velocity data. This also makes the method relatively insensitive to beam geometry and power intensity distribution.

As in the pressure-driven flow case, the major counter-ions to the negatively charged wall were those offered by the buffer solution. The resulting EDL thickness on the order 10 nm ensured that a flat electroosmotic velocity profile could be expected to extend right to the wall. Admittedly, there would be a steep velocity gradient in the EDL region, however, the thickness of the EDL prohibits resolution of this gradient with this or any other known velocimetry technique. This realization provided an opportunity to test the near-wall resolution of the present technique as follows: The point near the wall where the velocity profile falls from the electroosmotic velocity could be considered the closest significant datum.

A diffusion coefficient of $D = 4.37 \times 10^{-6}$ cm^2·s^{-1} was assigned, giving an electrophoretic mobility of $\nu_{ph} = -3.3 \times 10^{-4}$ cm^2·V^{-1}·s^{-1} as suggested by Harrison et al. [13] and Paul et al. [9]. Due to the negative charge of the uncaged dye ions, their net velocity was necessarily less than the underlying electroosmotic velocity.

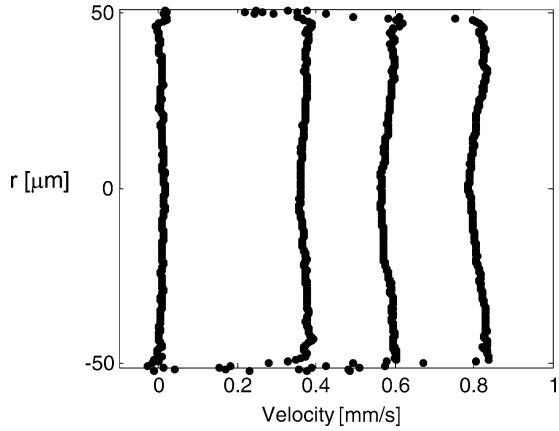

Fig. 5. Plots of velocity data from four electroosmotic flow experiments through a 102 μm i.d. capillary with applied electric field strengths of: 0 V/0.14 m; 1000 V/0.14 m; 1500/0.14 m; and 2000 V/0.14 m (from left to right).

Fig. 5 shows velocity data for the four flows corresponding to the image sequences in Fig. 4. Each velocity profile was calculated using an 8-image sequence and the numerical analysis technique. The velocity profile resulting from no applied field, appearing on the far left in Fig. 4, corresponds closely to stagnation as expected. This run also serves to illustrate that, despite significant transport of dye due to diffusion, the analysis method is able to recover the underlying stagnant flow velocity. Although the other velocity profiles resemble that of classical electroosmotic flow [5], a slight parabolic velocity deficit of approximately 4% was detected in all three flows. This was caused by a small backpressure induced by the electroosmotic fluid motion. In general, several factors can cause concave velocity profiles including:

a narrowing or partial blockage anywhere in the capillary; the presence of charged particles in the fluid; capillary forces resulting from different curvatures of the free surfaces in the reservoirs; contact angle hysteresis of a bubble entrapped in the channel; a non-uniform wall surface charge distribution; and slight height differences between the free surfaces in the reservoirs. Sensitivity to these factors is highly correlated with the capillary radius. In this case, it was evaluated that an adverse pressure gradient of only 50 $N{\cdot}m^{-3}$ would have been sufficient to generate the observed backflow. Such a pressure gradient could be easily generated if the height of one reservoir exceeded the other by less than 1 mm.

Velocity profiles plotted in Fig. 5 indicate electroosmotic wall velocities of 3.8×10^{-4} $m{\cdot}s^{-1}$, 6.0×10^{-4} $m{\cdot}s^{-1}$, and 8.2×10^{-4} $m{\cdot}s^{-1}$ (from left to right) giving electroosmotic mobility values of $\nu_E = 5.32 \times 10^{-4}$ $cm^2{\cdot}V^{-1}{\cdot}s^{-1}$, $\nu_E = 5.60 \times 10^{-4}$ $cm^2{\cdot}V^{-1}{\cdot}s^{-1}$, $\nu_E = 5.74 \times 10^{-4}$ $cm^2{\cdot}V^{-1}{\cdot}s^{-1}$, respectively. These values are in good agreement with $\nu_E = 5.07 \times 10^{-4}$ $cm^2{\cdot}V^{-1}{\cdot}s^{-1}$ in pH 8.0 reported by Paul et al. [9], and $\nu_E = 5.87 \times 10^{-4}$ $cm^2{\cdot}V^{-1}{\cdot}s^{-1}$ in pH 8.5 reported by Harrison et al. [13] (both in fused silica). From the average mobility calculated here, an effective zeta potential for this system is calculated to be $\zeta = -80$ mV. This is in keeping with silica oxide surfaces at KNO_3 concentrations near 10^{-2} M at pH 9.0 as reported by Hunter [5]. This is an improvement over the resolution achieved in the pressure-driven case (8 μm). This is because the two flows differ with respect to cross-stream velocity gradients, which induce radial concentration gradients and radial diffusion. In pressure-driven flow, the dye sample is distorted as shown in Fig. 3, which leads to increased radial diffusion (in addition to axial diffusion) and a loss of resolution. In electroosmotic flow, however, the sample is mostly translated with only axial diffusion acting to disperse the sample.

As in the pressure-driven flow case, all electroosmotic flow profiles exhibit a strong degree of symmetry. The velocity profile remains relatively flat for $-0.95 < r/R < 0.95$ in all cases. Due to the known, sub-micron thickness of the EDL, this range can be interpreted as confident velocimetry measurements up to $r/R = 0.95$, or 2.5 μm from the capillary wall. These results also provide experimental verification of the electroosmotic flow profile predicted in classical theory [5].

To illustrate repeatability, velocity data from three electroosmotic flows at an applied electrical field strength of 1000 V/0.14 m are superimposed in Fig. 6(a). Data near $r/R = -1$ is plotted in an expanded view in Fig. 6(b). The grouping of the velocity data from the three separate runs as well as the 2.5 μm near-wall resolution is readily apparent.

In future, retrieving fluorescent signal closer to the wall may be possible using channels of non-circular cross-section. Due to the angle between the inner sidewall and the optical axis, a closer index match between the solution and channel may also improve data acquisition near the wall (currently the capillary and the optical oil are well matched at $n_{ref} = 1.46$ and $n_{ref} = 1.485$, respectively, but the solution remains approximately that of water at $n_{ref} \approx 1.33$). As mentioned previously, a caged dye releasing a neutral marker would also be beneficial to the method. In lieu of that however, caged dyes releasing single component fluorescent molecules with predictable electrophoretic mobilities may be used.

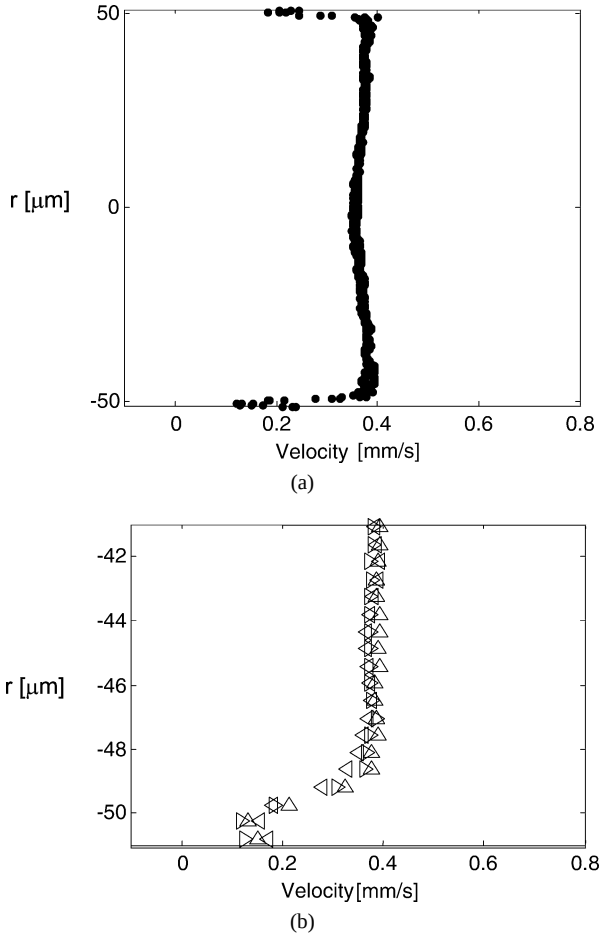

Fig. 6. Plots of velocity data taken from three electroosmotic flow experiments through a 102 μm i.d. capillary with an applied electric field strength of 1000 V/0.14 m: (a) Plotted over capillary cross-section; (b) Plotted in 10 μm leading up to the wall ($-0.8 > r/R > -1$).

4. Conclusions

A caged-dye based microflow visualization technique with near-wall resolution has been developed. An improved near-wall resolution over previous studies was the result of the optical system design and the multi-image analysis technique. The described optical system was designed to maximize signal reception and minimize distortion using high numerical aperture optics and complete oil immersion. The described analysis technique utilizes a multi-image sequence and calculates the cross-stream velocity profile based on an error-weighted average of the displacements of the concentration maxima profiles. The method was

first applied to pressure-driven flow through a 205 μm i.d. capillary. The measured velocity profile was in good agreement with the parabolic analytical solution up to 8 μm from each wall. The method was then applied to electroosmotic flow though a 102 μm i.d. capillary. In that case, the ability of the technique to determine fluid velocities up to 2.5 μm from the wall was demonstrated. This degree of accuracy was made possible by the combination of the optical system design and the image analysis technique described here.

Acknowledgement

Financial support of this work by the Natural Sciences and Engineering Research Council (NSERC) of Canada, through a postgraduate scholarship to D.S. and a research grant to D.L., is gratefully acknowledged.

References

[1] J.A. Taylor, E.S. Yeung, Imaging of hydrodynamic and electrokinetic flow profiles in capillaries, Anal. Chem. 65 (1993) 2928–2932.
[2] J.G. Santiago, S.T. Wereley, C.D. Meinhart, D.J. Beebe, R.J. Adrian, A particle image velocimetry system for microfluidics, Experiments Fluids 25 (1998) 316–319.
[3] C.D. Meinhart, S.T. Wereley, J.G. Santiago, PIV measurements of a microchannel flow, Experiments Fluids 27 (1999) 414–419.
[4] A.K. Singh, E.B. Cummings, D.J. Throckmorton, Fluorescent liposome flow markers for microscale particle-image velocimetry, Anal. Chem. 73 (2001) 1057–1061.
[5] R.J. Hunter, Zeta Potential in Colloid Science: Principles and Applications, Academic Press, New York, 1981.
[6] S.T. Wereley, C.D. Meinhart, Second-order accurate particle image velocimetry, Experiments Fluids 31 (2001) 258–268.
[7] T.J. Mitchison, K.E. Sawin, J.A. Theriot, K. Gee, A. Mallavarapu, Caged fluorescent probes, in: G. Marriot (Ed.), Caged Compounds, in: Methods in Enzymology, Vol. 291, Academic Press, New York, 1998, Chapter 4.
[8] W.R. Lempert, K. Magee, P. Ronney, K.R. Gee, R.P. Haugland, Flow tagging velocimetry in incompressible flow using photo-activated nonintrusive tracking of molecular motion (PHANTOMM), Experiments Fluids 18 (1995) 249–257.
[9] P.H. Paul, M.G. Garguilo, D.J. Rakestraw, Imaging of pressure- and electrokinetically driven flows through open capillaries, Anal. Chem. 70 (1998) 2459–2467.
[10] A.E. Herr, J.I. Molho, J.G. Santiago, M.G. Mungal, T.W. Kenny, M.G. Garguilo, Electroosmotic capillary flow with non-uniform zeta potential, Anal. Chem. 72 (2000) 1053–1057.
[11] W.J.A. Dahm, L.K. Su, K.B. Southerland, A scalar imaging technique for fully resolved four-dimensional vector velocity field measurements in turbulent flows, Phys. Fluids A 4 (10) (1992) 2191–2206.
[12] S. Inoue, K.R. Spring, Video Microscopy, the Fundamentals, 2nd Edition, Plenum, New York, 1997.
[13] D.J. Harrison, A. Manz, Z. Fan, H. Ludi, M. Widmer, Capillary electrophoresis and sample injection systems integrated on a planar glass chip, Anal. Chem. 64 (1992) 1926–1932.